TECHNICAL REPORT No. 17

THE RESPONSE OF A GLOBAL BAROTROPIC MODEL TO FORCING BY LARGE-SCALE OROGRAPHY

by

J. Quiby

January 1980

£1.00

CONTENTS

	Page
Abstract	i
1. DESCRIPTION OF THE MODEL	1
1.1 Introduction	1
1.2 The model equations	2
1.3 The spatial differencing scheme	4
1.4 Modification of the spatial differencing scheme and at the poles	4
1.5 The time-stepping scheme and the time filter	7
1.6 Space filter	7
1.7 Linear diffusion	8
1.8 Linear drag	8
2. DESCRIPTION OF THE EXPERIMENTS	9
2.1 Preliminary remarks	9
2.2 Experiment 1: Solid rotation	10
2.3 Experiment 2: Idealized zonal flow	16
2.4 Experiment 3: Climatological zonal flow	20
2.5 Concluding remarks	27
Acknowledgements	27
References	29

Abstract

The large-scale effects of mountainous massifs are investigated with a global shallow water equation model whose finite difference formulation exactly conserves potential absolute enstrophy. At first, the perturbations caused by a circular mountain to two different idealized zonal flows are investigated. Then the 300-mbar zonal flow longitudinally averaged for the winter is considered. The perturbations brought to this flow by the global orography are compared with climatology and with the response obtained, in a similar work, by Grose and Hoskins (1979).

---

1. DESCRIPTION OF THE MODEL

1.1 Introduction

Charney and Eliassen (1949) published the first study on the influence of large scale orography upon atmospheric motions. They showed in their paper that the large scale quasi-stationary disturbances in the mid-latitude westerlies are due to continental elevations. They draw this conclusion from the results of an equivalent barotropic model including orography and surface friction.

This pioneering work has been followed by numerous studies. When baroclinic models became available, it also became possible to simulate a thermal forcing and therefore to investigate either the respective or the combined effects of these two forcings. More recently, tests have been carried out with full general circulation models.

The advantage of using a shallow water equation model to study the dynamical effects of orography upon atmospheric motions is that the response is solely and unequivocally due to orographic features and is not biased by the thermal structure. This latter determines the vertical stability and, indirectly, the vertical wind shear. Considering the broad range of variation of these parameters, they would presumably considerably differentiate the responses. As we are, in this work, first of all interested in the large-scale effects of the largest mountainous massifs of the earth, the most appropriate geometry is the global one.

A very similar study has been made by Grose and Hoskins (1979) who solved the steady state linear shallow water equations on the sphere by expansion of the dependent variables in truncated spherical harmonics. The results obtained by these two authors will be compared with those shown in this study.

The model described in this note has been derived from an earlier model - developed by Robert Sadourny - that has been used as a forerunner for the ECMWF baroclinic model. It is very similar to this latter model, as far as a shallow water equation model can resemble a multi-layer baroclinic model. It has the same grid, the same spatial differencing scheme for the equations of motion (if we except the additional pressure term due to the sigma coordinates and the term involving the vertical coupling),

the same treatment of the polar singularities, the same time-stepping scheme with the same time filter. A difference is to be found in the space filter. The tendencies of all the historical variables are Fourier filtered in the main model. In the barotropic one, only the geopotential (the variable, not its tendency) is Fourier filtered. Because of these similarities, the description of the barotropic model has been limited to a minimum and the interested reader is asked to consult the detailed documentation prepared by Burridge and Haseler (1977) and Haseler and Burridge (1977) for the ECMWF baroclinic model.

1.2 The model equations

Expressed for a β-plane, the shallow water equations without orography have the following form:

$$\frac{\partial u}{\partial t} = - u \frac{\partial u}{\partial x} - v \frac{\partial u}{\partial y} - \frac{\partial \phi}{\partial x} + fv$$

$$\frac{\partial v}{\partial t} = - u \frac{\partial v}{\partial x} - v \frac{\partial v}{\partial y} - \frac{\partial \phi}{\partial y} - fu$$

$$\frac{\partial \phi}{\partial t} = - \frac{\partial}{\partial x}(u\phi) - \frac{\partial}{\partial y}(v\phi)$$

All the symbols used have their usual meaning (see the List of Symbols on the next page).

It is well known that the above set of equations satisfies the following constraints for an integration over the whole globe.

$$\frac{\partial}{\partial t} \int \phi \, ds = 0$$ Conservation of mass

$$\frac{\partial}{\partial t} \int \frac{1}{2}(\phi^2 + E\,\phi) ds = 0$$ Conservation of the total energy

$$\frac{\partial}{\partial t} \int \frac{(\zeta + f)^2}{\phi} ds = 0$$ Conservation of the potential absolute enstrophy

List of Symbols

u	=	longitudinal (or zonal) velocity
v	=	latitudinal (or meridional) velocity
h	=	height of the free surface
g	=	gravity acceleration
ϕ	=	geopotential of the free surface ($\phi = gh$)
H	=	height of the orography
f	=	Coriolis parameter
β	=	df/dy
ζ	=	relative vorticity
λ	=	longitude
θ	=	latitude
a	=	earth's radius
IM	=	number of longitudinal points
K	=	diffusion coefficient
C	=	drag coefficient
E	=	$u^2 + v^2$

1.3 The spatial differencing scheme

The spatial differencing scheme used is the one devised by Sadourny (1975a,b) which strictly conserves the mass and the potential absolute enstrophy for the Arakawa C grid.

The equations are expressed in spherical coordinates; the orography is included in the continuity equation.

$$\frac{\partial u}{\partial t} = \overline{Z}^{\theta} \frac{\overline{V}^{\theta\lambda}}{\cos\theta} - \frac{1}{a\cos\theta}\,\delta_{\lambda} P$$

$$\frac{\partial v}{\partial t} = -\,\overline{Z}^{\lambda}\,\overline{U}^{\theta\lambda} - \frac{1}{a}\,\delta_{\theta} P$$

$$\frac{\partial \phi}{\partial t} = -\frac{1}{a\cos\theta}\left\{\delta_{\lambda}\,(U - ug\overline{H}^{\lambda})\right\} - \frac{1}{a\cos\theta}\left\{\delta_{\theta}\,(V - vg\overline{H}^{\theta}\cos\theta)\right\}$$

$$U = \overline{\phi}^{\lambda}\, u \qquad\qquad V = \overline{\phi}^{\theta}\, v\cos\theta$$

$$Z = \frac{1}{\overline{\phi}^{\theta\lambda}\, a\cos\theta}\left\{\delta_{\lambda} v - \delta_{\theta}(u\cos\theta) + af\cos\theta\right\}$$

$$P = \phi + \frac{1}{2}\left\{\overline{u^2}^{\lambda} + \frac{1}{\cos\theta}\,\overline{v^2\cos\theta}^{\theta}\right\}$$

$$f = 2\Omega\sin\theta$$

1.4 Modification of the spatial differencing scheme near and at the poles

u and v are not defined at the poles. But the geopotential ϕ is defined, thus its tendency $\frac{\partial \phi}{\partial t}$ has to be computed.

Computation of $\frac{\partial \phi}{\partial t}$

The theorem of the divergence or Gauss' theorem is used.

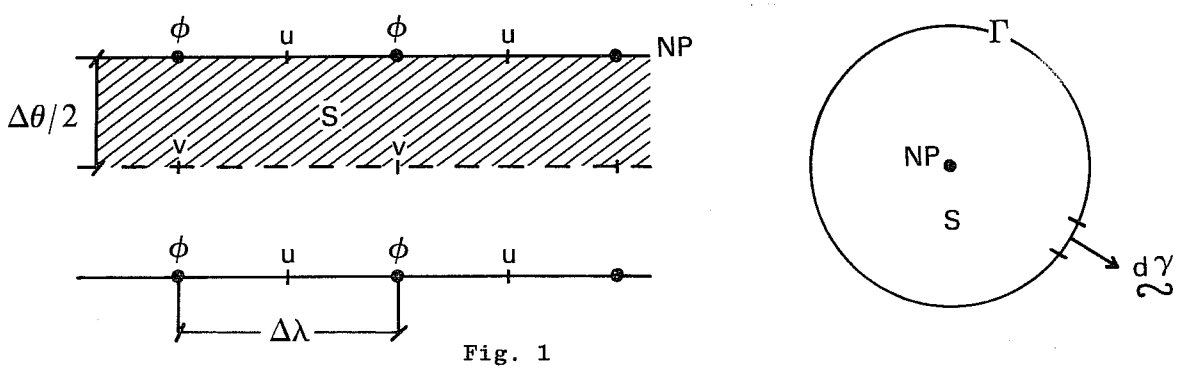

Fig. 1

$$\int_S \text{div}\,\{(\phi - gH)\underset{\sim}{V}\}\,ds = \oint_\Gamma (\phi - gH)\underset{\sim}{V} \cdot d\underset{\sim}{\gamma}$$

For the North-Pole (NP), we have (Fig. 1)

$$\text{div}\,\{(\phi - gH)\underset{\sim}{V}\}_{NP}$$

$$= -\frac{1}{S}\sum_{I=1}^{IM} (\phi - gH)(I)\cdot v(I)\cdot a \sin\frac{\Delta\theta}{2}\cdot\Delta\lambda$$

S = surface of the polar cap
IM = number of longitudinal points

With the help of the continuity equation

$$\frac{\partial}{\partial t}\{\phi\}_{NP} = -\,\text{div}\,\{(\phi - gH)\underset{\sim}{V}\}_{NP}$$

it becomes:

$$\frac{\partial}{\partial t}\{\phi\}_{NP} = -\frac{1}{S}\sum_{I=1}^{IM} \overline{(\phi - gH)}^{\theta}(I)\cdot v(I)\cdot a \sin\frac{\Delta\theta}{2}\cdot\Delta\lambda$$

The same treatment applies at the South-Pole as well.

For the computation of $\frac{\partial v}{\partial t}$ at a distance $\frac{\Delta\theta}{2}$ from the pole (the first v-line after the NP-line and the last v-line before the SP-line), we need to know U and P at the poles.

Boundary condition for the mass-flux U at the poles

1. $\sum_{I=1}^{IM} U(I)=0$ (1) because if $u(\lambda)$ - as well as $v(\lambda)$ - has to be defined at the pole, it must vary as a sine for continuity reasons.

2. We impose:

$$\text{div}\,\{(\phi - gH)\underset{\sim}{V}\}_{NP}$$

$$= \frac{1}{S}\oint_\Gamma (\phi - gH)\underset{\sim}{V}\cdot d\underset{\sim}{\gamma} = \frac{1}{S}\oint_c (\phi - gH)\underset{\sim}{V}\cdot d\underset{\sim}{\gamma}'$$

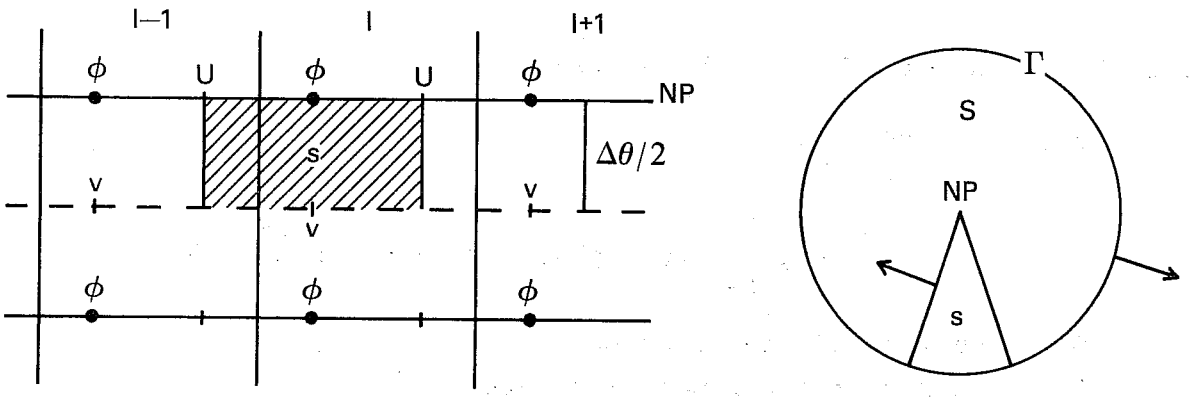

Fig. 2

The equality

$$\oint_c (\phi - gH)\underset{\sim}{V} \cdot d\underset{\sim}{\gamma}' = \frac{s}{S} \oint_\Gamma (\phi - gH)\underset{\sim}{V} \cdot d\underset{\sim}{\gamma}$$

yields the relation (see Fig. 2)

$$\{U(I) - U(I-1)\} \frac{\Delta\theta}{2} = \overline{(\phi - gH)}^{\theta}(I) \cdot v(I) \cdot \sin\frac{\Delta\theta}{2} \cdot \Delta\lambda -$$

$$- \frac{s}{S} \sum_{I=1}^{IM} \overline{(\phi - gH)}^{\theta}(I) \cdot v(I) \cdot \sin\frac{\Delta\theta}{2} \cdot \Delta\lambda$$

if we suppose that, at the poles, $H \ll h$. This assumption is perfectly correct at the North Pole, but is very bad at the South Pole. It is nevertheless necessary if we want to use the same boundary condition as in the baroclinic model.

Relations (1) and (2) allow to compute the IM values U(I). So computed, the U(I) are not necessarily of the form sine of λ because at the poles the U(I) are not true velocity variables. The same procedure is used at the South Pole.

Boundary condition for the auxiliary potential P at the poles

We suppose a homogeneous flow crossing the polar cap.

We want to know at the pole:

$$P = \phi + \frac{1}{2} E \text{ where } E = u^2 + v^2$$

By considering that

$$v(\lambda) = \sqrt{E} \sin \lambda$$

it comes that

$$E = \frac{1}{\pi} \int_0^{2\pi} v^2(\lambda) d\lambda$$

$$\therefore P = \phi + \frac{1}{IM} \sum_{I=1}^{IM} v^2 (I)$$

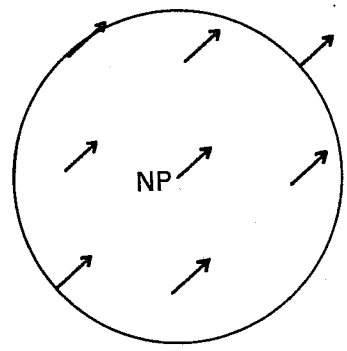

Fig. 3

The v(I) are taken at a distance $\frac{\Delta\theta}{2}$ from the poles (see Fig. 3).

For the computation of Z on the first and last v-lines, the values of u at the poles are needed. They are set equal to zero and remain zero through the whole integration.

1.5 The time-stepping scheme and the time filter

The time-stepping scheme is a leapfrog scheme for the dynamics and a forward step for the linear drag and the linear diffusion.

A time-filter of type Asselin (1972) is used with the three dependent variables. Example with u:

$$u^*(T) = u(T) + \varepsilon\{u(T+1) - 2u(T) + u^*(T-1)\}$$

1.6 Space filter

Latitudinally dependent Fourier filtering of the geopotential and of the auxiliary potential P.

The filtering scheme has been designed so that the stability criterion for the finite difference scheme can be based on the longitudinal grid length at some fixed latitude and the filter is then applied polewards of this latitude in both hemispheres (Burridge and Haseler 1977 and Haseler and Burridge 1977).

1.7 Linear diffusion

A linear second order horizontal diffusion acts on all the variables.

$$\frac{\partial u}{\partial t} = ... + K \nabla^2 u$$

$$\frac{\partial v}{\partial t} = ... + K \nabla^2 v$$

$$\frac{\partial \phi}{\partial t} = ... + K \nabla^2 \phi$$

The same coefficient K is used for each variable. The Laplacian ∇^2 has the form:

$$\nabla^2 \eta = \frac{1}{a^2 \cos^2\theta} \cdot \overline{\delta_\lambda \{ \overline{\delta_\lambda \eta}^{\theta} \}}^{\theta} + \frac{tg\theta}{a^2} \overline{\delta_\theta \eta}^{\theta} + \frac{1}{a^2} \overline{\delta_\theta \{ \overline{\delta_\theta u}^{\lambda} \}}^{\lambda}$$

1.8 Linear drag

A linear drag acts on the velocity

$$\frac{\partial u}{\partial t} = ... - Cu$$

$$\frac{\partial v}{\partial t} = ... - Cv$$

Same coefficient C is used for u and v.

2. DESCRIPTION OF THE EXPERIMENTS

2.1 Preliminary remarks

All the experiments described hereafter have been carried out with the following parameter values:

Resolution: N24 (3.75 degrees)

Timestep: 5 minutes

Average height of the free surface: 7000 m

Time-filter coefficient: $\varepsilon = 0.001$

The space-filter starts at the Equator

Diffusion coefficient: $K = 0.0$ (no diffusion)

or $K = 3.0 \cdot 10^5 \ m^2 s^{-1}$ (with diffusion)

Orography:

Isolated mountain:

circular, $\cos^2$-shaped, height: 3000 m,
radius of the base: 20^o (2224 km).

Planetary orography:

As described in Experiment 3.

Growing rate of the orography: 3 days.
The orography begins to grow not at the start of the integration but 24 hours later, when the wind field is very well balanced with the mass field. Tests with orography developing from the start of the integration were noisier than the ones with a delayed growth of the orography.

Initialisation:

The wind field is given. A balanced mass field is obtained by solving the reverse linear balance equation.

2.2 Experiment 1: Solid rotation

In an unperturbed zonal wind rotating as a solid body with a maximal tangential velocity of 18 ms^{-1} (Fig. 4), there grows in three days at latitude 30 ^{o}N a circular mountain. After an integration of 10 days - that is to say 6 days after orography has reached its full height - the perturbation brought about to the flow by this obstacle is reproduced in Fig. 5. Fig. 6 shows the same perturbed flow after 15 days. (This integration is performed without diffusion).

The anticyclonic curvature of the contour lines over the mountain is explained by the conservation of the potential absolute vorticity:

$$\frac{D}{Dt}\left(\frac{\zeta+f}{h-H}\right) = 0$$

As pressure gradients must be very weak close to the equator, a pressure chart (in our case the height of the free surface) does not give a good account of the waves in the tropics. It is better to look at the wind field. Fig. 7 and Fig. 8 depict the relative vorticity after 10 and 15 days of integration, respectively.

When these charts are compared with the perturbation vorticity map in the work of Grose and Hoskins (Fig. 3a in Grose and Hoskins, 1979), we also note an anticyclone upslope of and over the mountain, a downslope cyclone, a train of waves downstream of the mountain exhibiting a strong northeast-southwest tilting. This wavetrain splits into a double structure in latitude. What is less marked in the present study is the reinforcement in the antipodean region and the reversing of the tilting of the wave after it has passed the antipodean point.

Very similar patterns to Fig. 7 and Fig. 8 have been obtained by plotting the wind component v.

The difference between the 10 day integration (Fig. 5) and the 15 day one (Fig. 6) shows the propagation of the wave.

It could be interesting to compare the response on a sphere with the one in a channel. Kasahara (1966) placed a circular obstacle of parabolic shape in the middle of a channel at 45 ^{o}N.

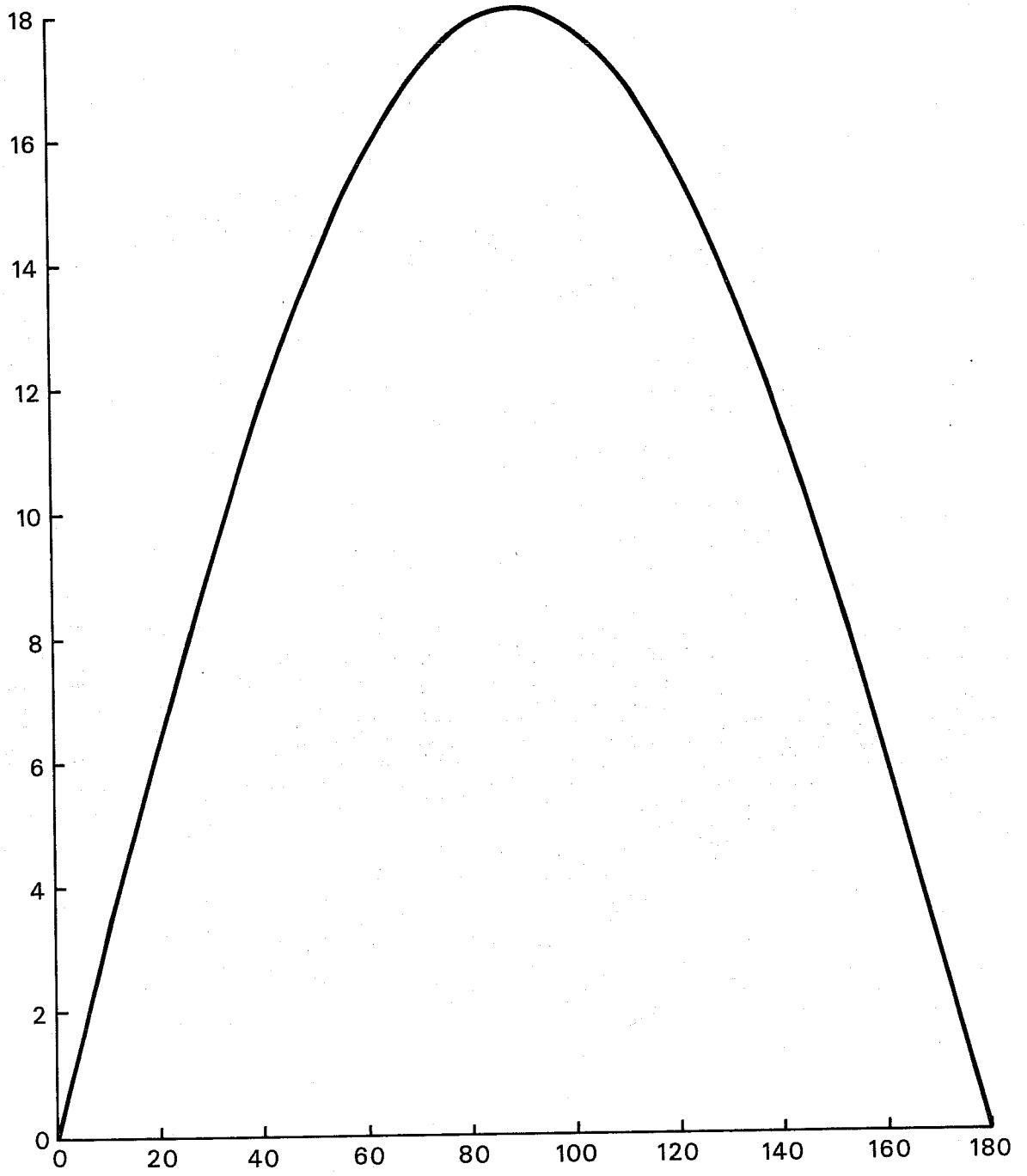

Fig. 4 Initial meridional profile of the zonal wind for the solid rotation case. Ordinate: wind velocity in ms^{-1}. Abscissa: colatitude.

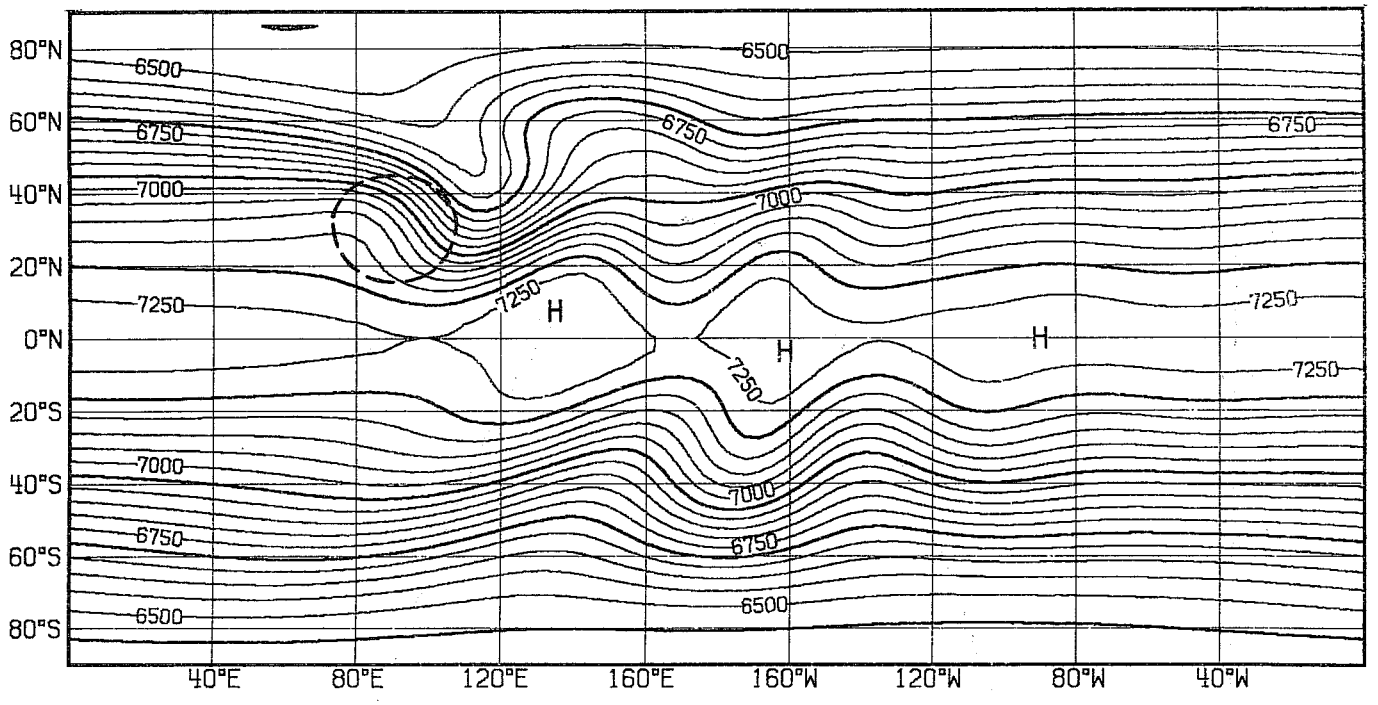

Fig. 5 Height in m of the free surface at day 10 for the solid rotation case. The dashed line shows the position of the obstacle.

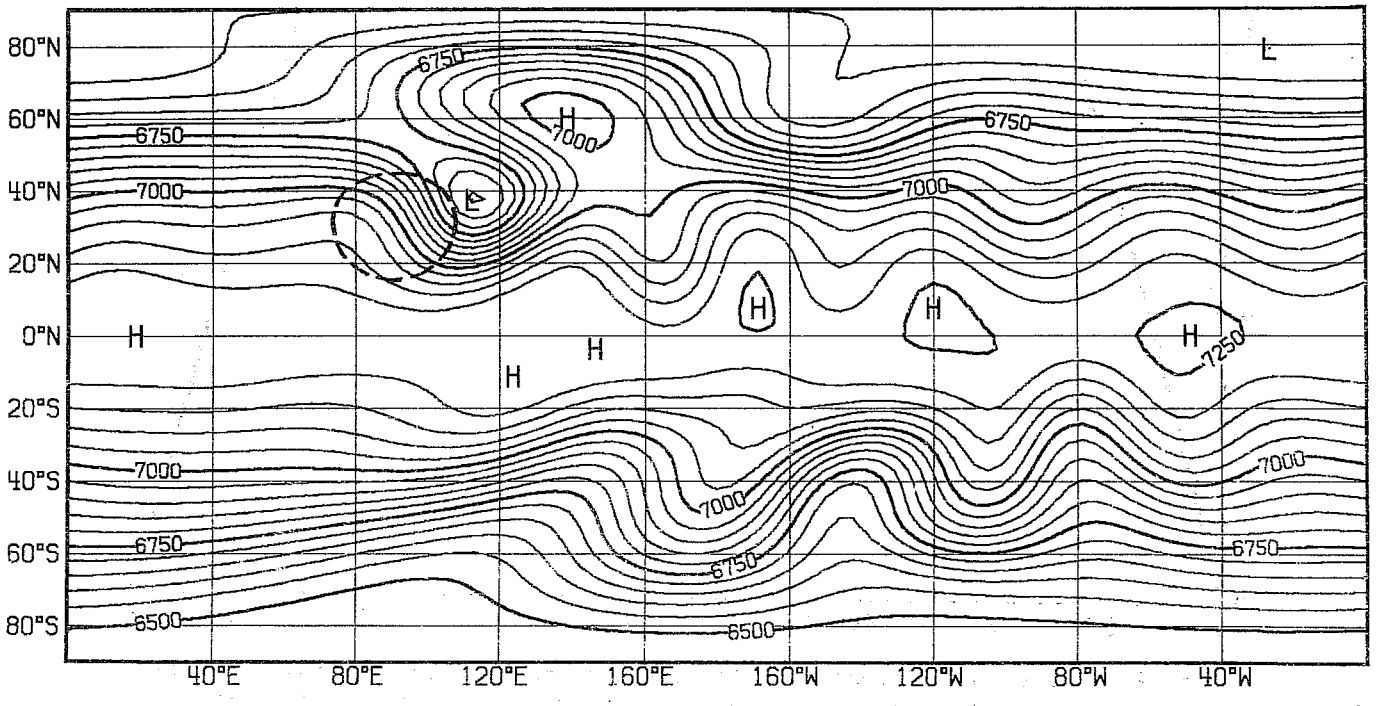

Fig. 6 Same as Fig. 5 but at day 15.

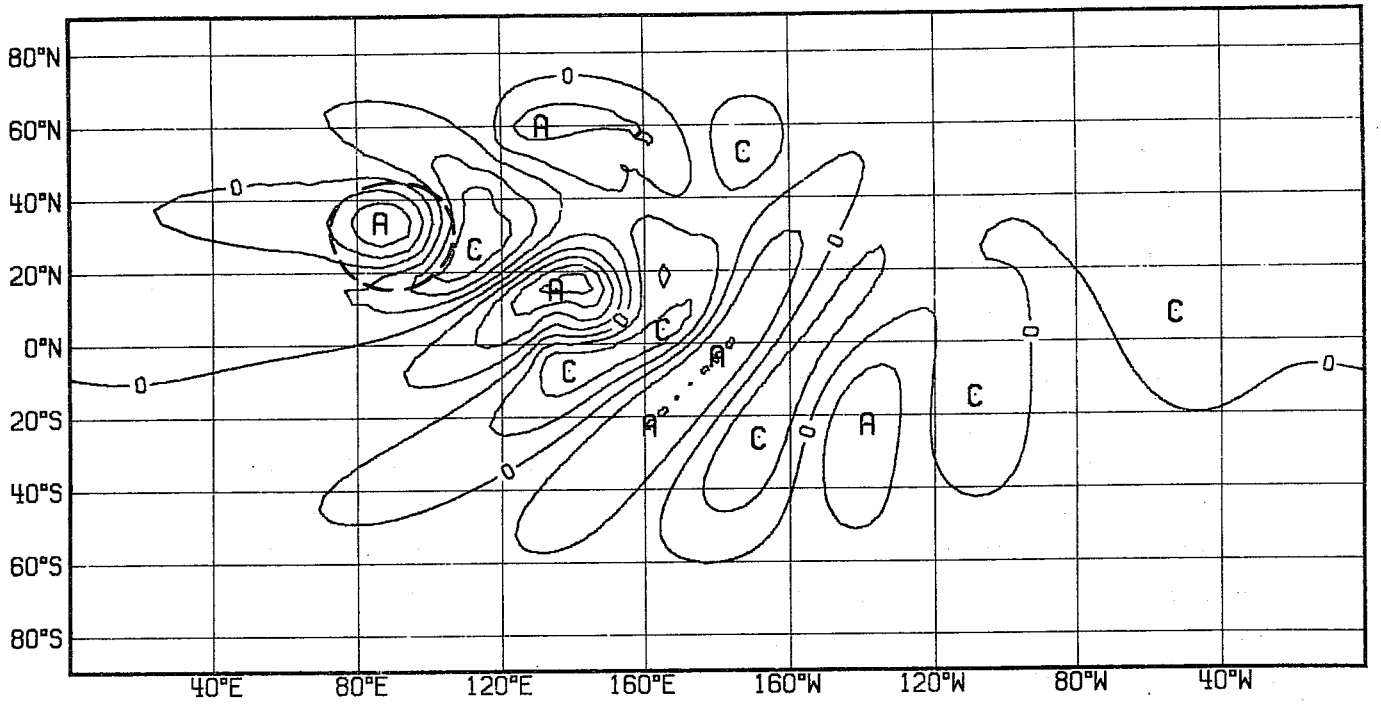

Fig. 7 Relative vorticity field after 10 days for the solid rotation experiment. Vorticity * 10^5. Intervals: $1s^{-1}$.

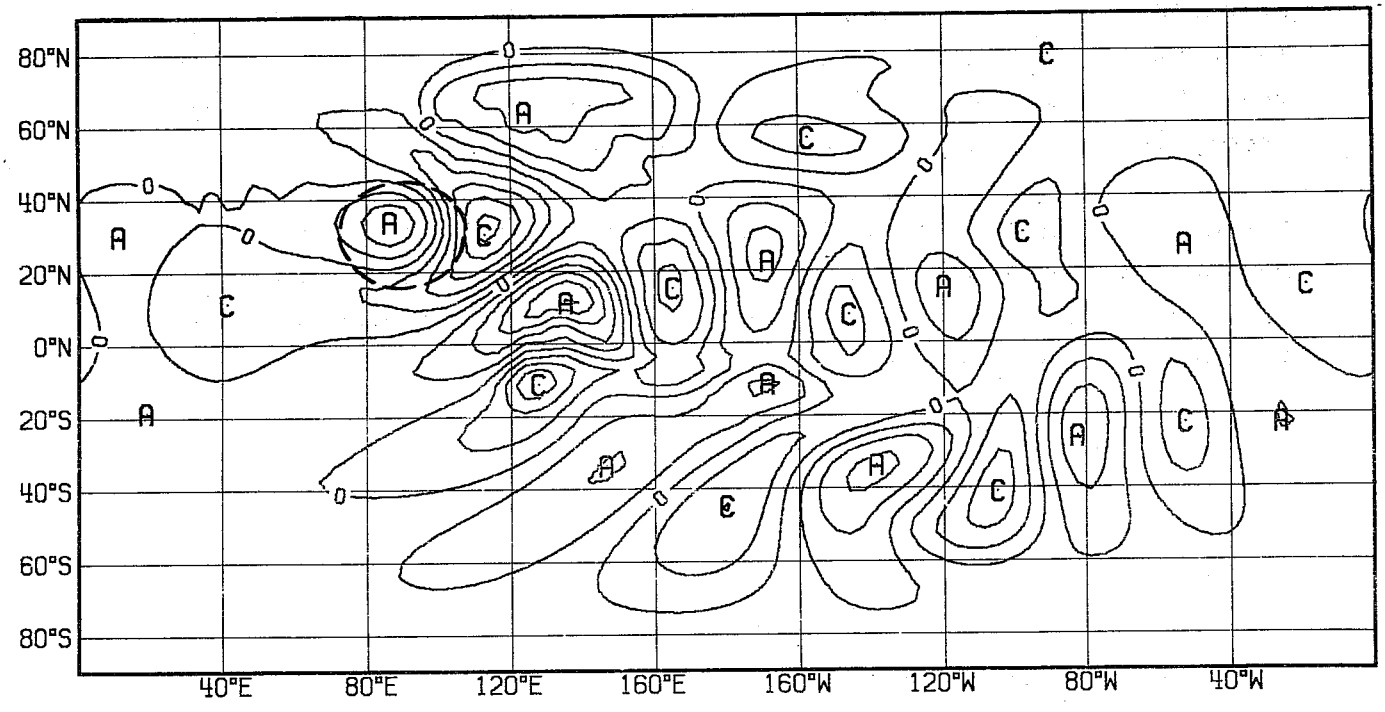

Fig. 8 Same as Fig. 7 but after 15 days.

Height of the obstacle: 2000 m

Radius of its base: 1769 km

Width of the channel: 7075 km

Average height of the free surface: 7000 m

Zonal flow velocity: 20 ms^{-1}

Between 8 and 14 days of integration with full height of the obstacle from the start, the perturbation was a wave 3 (Fig. 9). In the present experiment, we have at 10 days 3 very well marked waves in the free surface contour chart, with a weak fourth wave (Fig. 5). The vorticity pattern (Fig. 7) shows 4 waves with a weak fifth maximum. At 15 days, a wave 6 has established, recognisable on the free surface chart (Fig. 6) as well as on the relative vorticity chart (Fig. 8).

It may also be of interest to see how the waves generated by an isolated mountain compare with the theory of the Rossby-Haurwitz waves (Haurwitz, 1940 summarised in Haltiner and Martin, 1957). These waves are a generalisation of the Rossby waves in the sense that they no longer must be of infinite lateral extent. But this theory is valid for a channel on a β-plane, not for a sphere.

Moreover it has been derived from the linearized equations of motion and requires a horizontal divergence everywhere equal to zero, two conditions which are not satisfied in the present experiment. According to Haurwitz, we have:

$$c = U - \frac{\beta L^2}{\pi^2 (4 + \frac{L^2}{4d^2})}$$

where

$\beta = df/dy$

U = velocity of the basic zonal flow

c = phase-speed of the wave

L = wave-length

d = half width of the channel (At $y = \pm d$, $v = 0$)

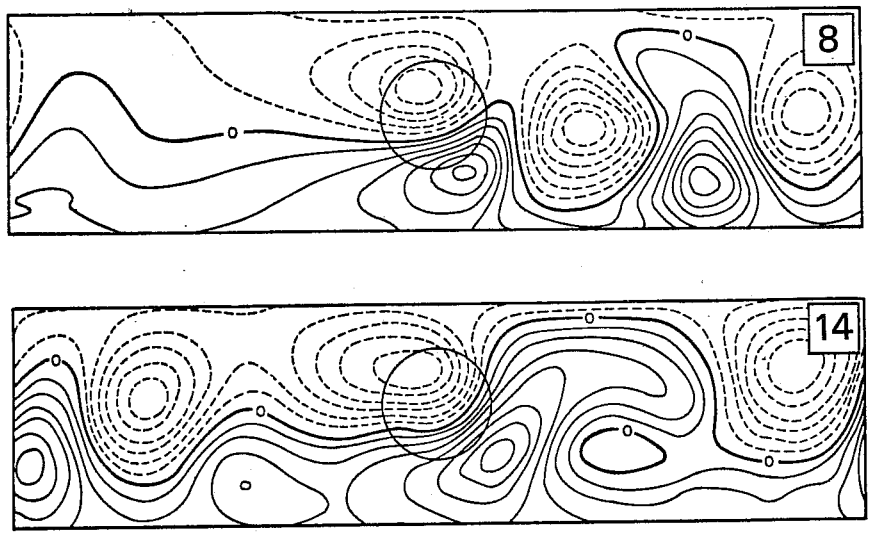

Fig. 9 Contour patterns at day 8 and 14 of the height deviation from the initial height of the free surface. Contours drawn every 50 m. Dashed contours: positive deviation. Solid contours: negative deviation. The circular obstacle is shown by a circle. (After Kasahara).

We shall consider the flow at 15 days as stationary and shall compute the number of waves. It comes:

$$L^2 = \frac{4\pi^2 U}{\beta - \frac{\pi^2 U}{4d^2}}$$

$2\pi a \cos(30^o)/L$ = number of waves

U = mean zonal wind at 30 ^oN at day 15

$U = 11.9\ ms^{-1}$

$\beta(30\ ^oN) = 9.913 \cdot 10^{-12}\ m^{-1}s^{-1}$

d = distance 30 ^oN - North Pole

$d = 6.667 \cdot 10^6$ m

a = earth's radius

$a = 6371 \cdot 10^3$ m

With these values, the number of waves is 5 (4.9 more precisely). As we observe 6 waves, the agreement is surprisingly good for a spherical geometry.

2.3 Experiment 2: Idealized zonal flow

The same circular mountain is placed in an idealized westerly zonal flow which is maximum (18 ms^{-1}) at 45^o of latitude in both hemispheres and zero at the Poles and at the Equator (Fig. 10).

Fig. 11 and Fig. 12 show the resulting perturbation respectively in the height field and in the vorticity field after 10 days. In Grose and Hoskins (1979), the authors arrive at the conclusion that "the equatorial easterlies provide an effective barrier for stationary waves". It seems that a zero wind at the Equator already prevents perturbations from entering into the Southern Hemisphere (compare Fig. 7 with Fig. 12).

Fig. 12 shows a much shorter wavetrain than in the three perturbation vorticity charts of Fig. 4 in Grose and Hoskins (1979) even when it is compared with the J3 case (300 mbar summer). This could be due to the fact that 10 days of integration is too short a period of time for comparison with the steady state. Experiment 1 shows

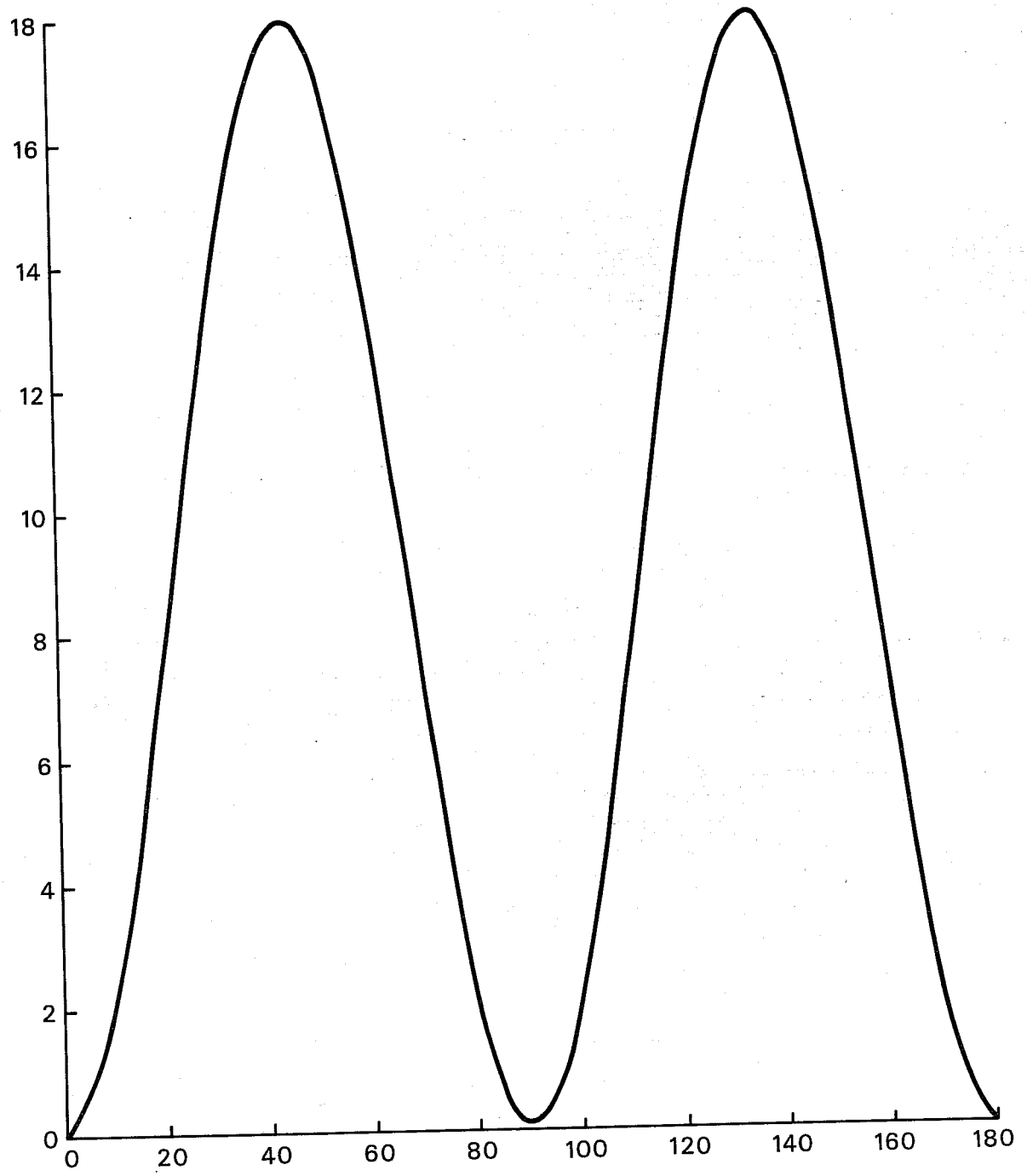

Fig. 10 Initial meridional profile of the zonal wind for Experiment 2.
Ordinate: wind velocity in ms^{-1}. Abscissa: colatitude.

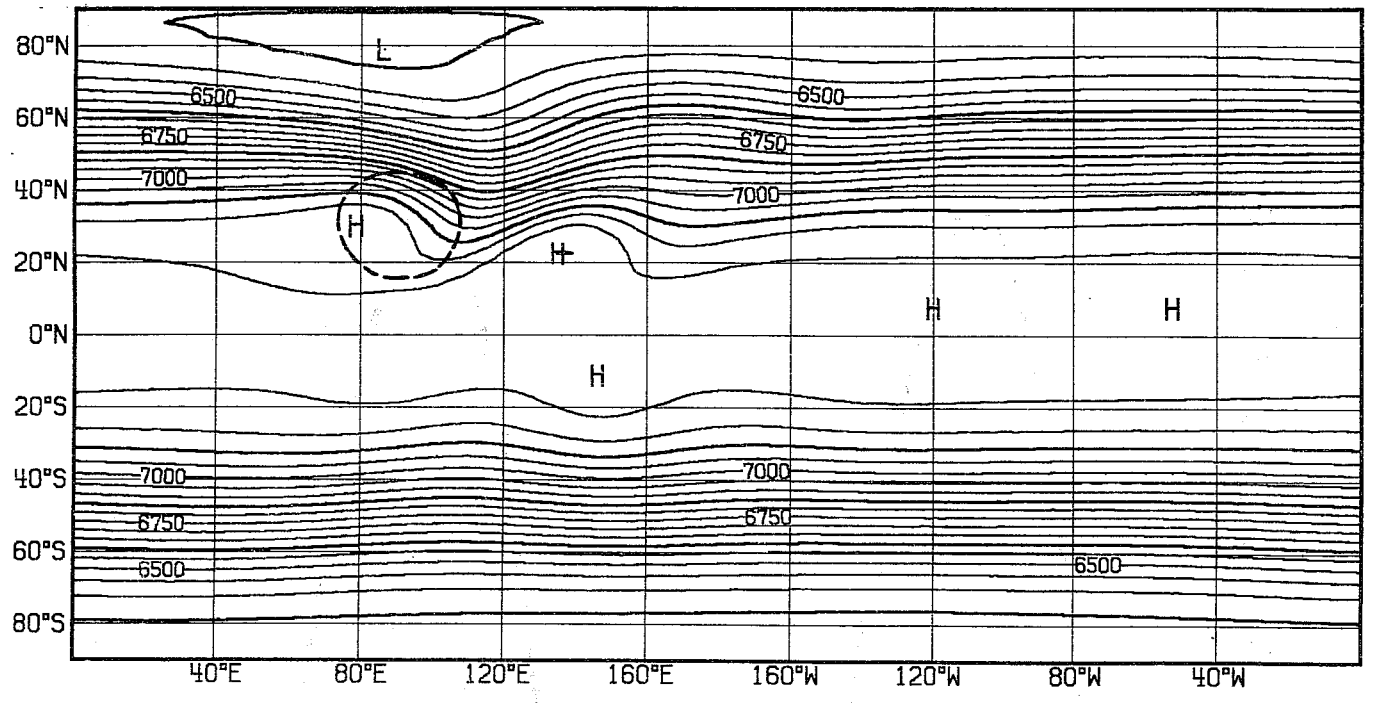

Fig. 11 Height in m of the free surface at day 10 in Experiment 2.
The dashed line shows the position of the circular mountain.

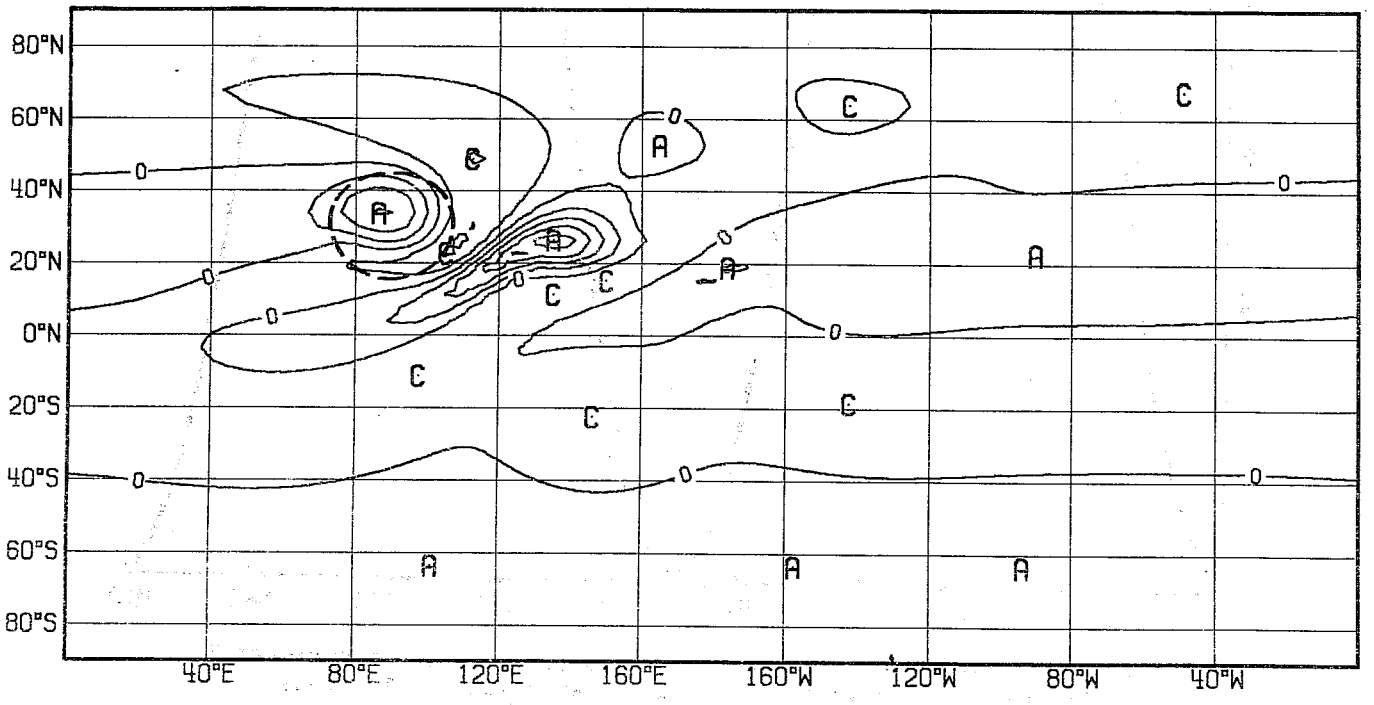

Fig. 12 Relative vorticity field after 10 days for Experiment 2.
Vorticity * 10^5. Intervals: $1s^{-1}$.

that the "best fit" with the steady state solution lies between 10 and 15 days.

It is not irrelevant to compare also the absolute contour height field (Fig. 11) with the total stream function maps of Fig. 4 in Grose and Hoskins (1979). We obviously have to remember that the stream function leaves out the divergent part of the wind. As, in the experiment under review, it is only over the mountain that the divergence exceeds $\pm 1.0 \cdot 10^{-6}$ s^{-1} (maximum $< 5.0 \cdot 10^{-6}$ s^{-1} on the windward slope, minimum $> -3.0 \cdot 10^{-6}$ s^{-1} on the lee side), both fields can be compared if the tropical and mountainous regions are disregarded. Thus, we also have a strongly tilted trough just behind the mountain, an anticyclone between 40^{o} and 60^{o} downstream from the mountain and there is a slight ridge to the north and a trough to the south at about 80^{o} downstream.

Circular mountain at the latitude 60 ^{o}N

When the same circular mountain lies at 60 ^{o}N, the main feature to be seen in the contour height field (not shown) is a split of the zonal current into two streams, one circulating to the north of the obstacle, the other to its south. On the eastern slope of the obstacle, the northern current turns equatorwards until it merges with the southern current. This creates a closed depression to the east-northeast of the mountain, 60^{o} - 100^{o} downstream from it. By looking at the relative vorticity field (not shown), we note, as in Grose and Hoskins (1979), "a large vorticity response near the mountain and a strongly east-northeast to south-southwest tilted wavetrain. The waves display no splitting tendency".

This experiment with the mountain at 60^{o}N has been repeated without diffusion. Some irregularities (noise) have been found in the relative vorticity field, first of all in the area of the mountain, and, to a much less extent, in the free surface height in the vicinity of the North Pole.

2.4 Experiment 3: Climatological zonal flow

This experiment shows the response of a climatological zonal flow to the global orography.

A. The planetary orography

This orography has been derived from the N48 GFDL orography, the construction of which is explained in Holloway and Manabe (1971). It is a smooth orography where large massifs like Himalaya or Antartica are well represented. On the contrary, high ridges as the Rocky Mountains or the Andes see their altitude strongly reduced. This leads to a misrepresentation of the barrier-effect they actually produce on atmospheric flows (Fig. 13). This shortcoming is inherent to every orography defined by spatial averaging over a coarse mesh.

Maximum height of some mountains:

Alps	496 m
Greenland	2262 m
Rocky Mountains	2221 m
Himalaya	5093 m
Andes	2634 m
Antartica	4065 m

B. The climatolgical zonal flow

For the Northern Hemisphere, the mean zonal wind in winter for the 500 mb surface computed by Oort and Rasmusson (1971) has been used. The values are averages from the North Pole to 10 degrees south. For the Southern Hemisphere, the meridional profile of the zonal wind at 500 mb has been read out from a mean zonal wind diagram derived by Newell et al (1969). (Fig. 14).

C. The experiment

For this experiment, the diffusion coefficient is $K = 3.0 \cdot 10^5$. Fig. 15 and Fig. 16 show the response of the free surface and of the wind field on a global cylindrical projection after 10 days and Fig. 17 also shows the response of the free surface after 10 days, but on a stereographic projection for the Northern Hemisphere. Startling is the difference between the Northern and the Southern Hemisphere: a very perturbed flow has developed in the Northern one, a slightly disturbed one in the Southern.

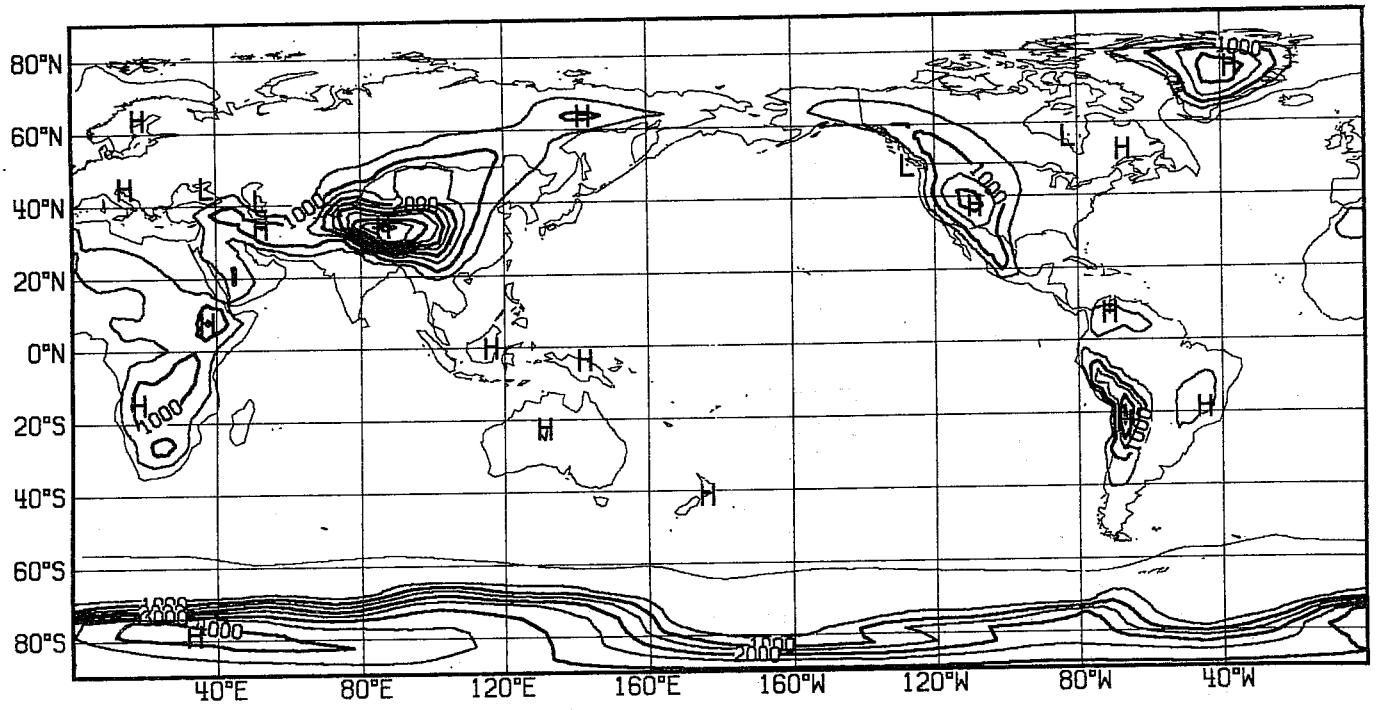

Fig. 13 Global orography. Line intervals: 500 m.

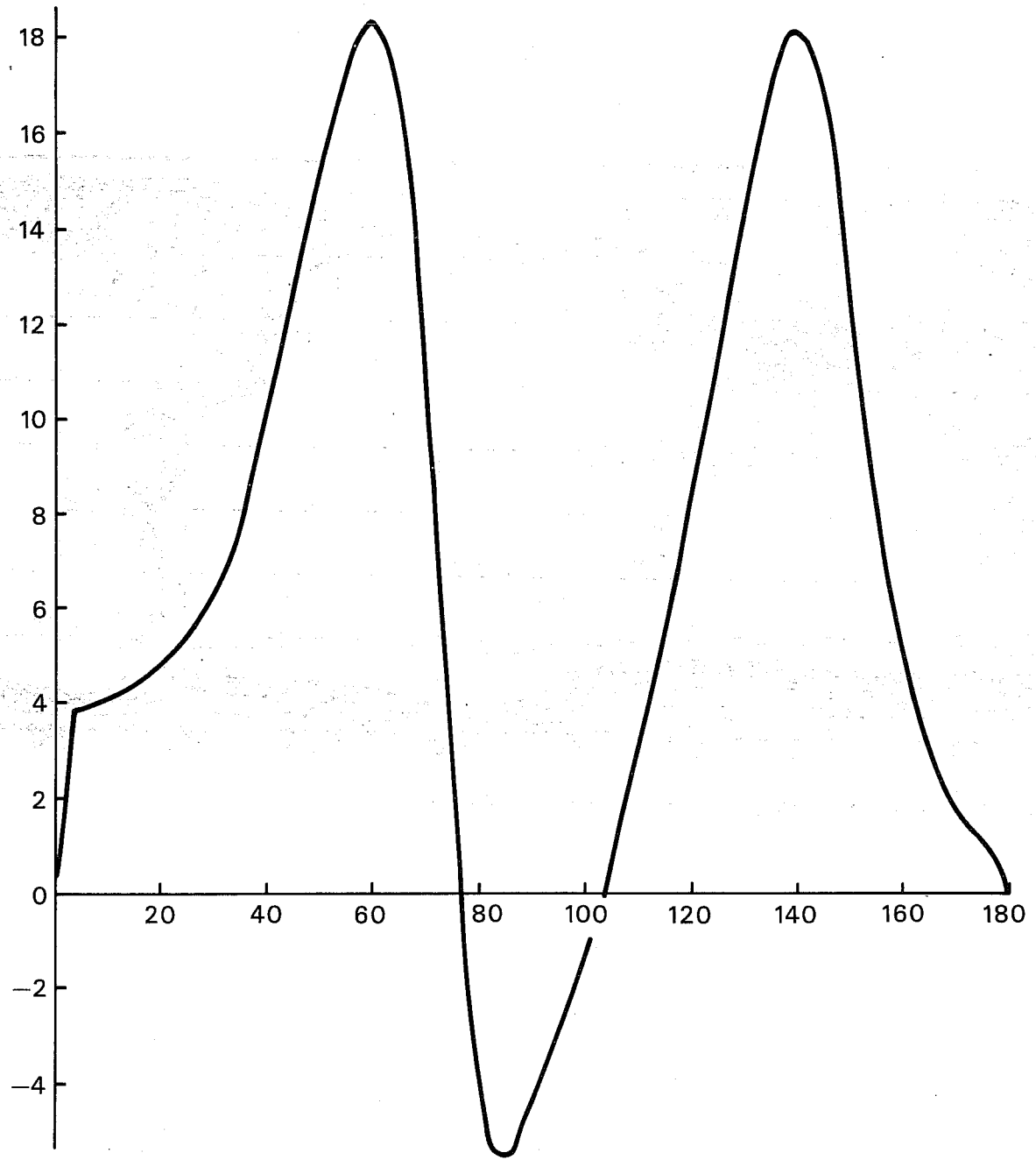

Fig. 14 Climatological mean zonal wind. Ordinate: wind velocity in ms^{-1}. Abscissa: colatitude.

This is mainly due to the northern position of the highest part of the Andes (20S) and the southern position (50S) of the peak of the average zonal wind (Fig. 14). Noticeable on Fig. 16 are three anticyclonic cells at about 20 ^{o}N. This could suggest a reinforcement by the orography of the anticyclones of the high pressure belt.

It would be nice to compare the results of the model with reality. But the atmosphere has no free surface as a barotropic model does! Thus a comparison has been made with a 500-mbar climatology (Neiburger, Edinger and Bonner, 1971) (Fig. 18). This climatology has been found very similar to two others (Dzerdzeevskii and Pogosyna, 1968, and Barry and Perry, 1973) and will thus be considered as reference. It has to be noticed that the average 500 mbar surface shows a pattern practically identical to that of the climatology of the 300 mbar surface height in winter. (This resemblance is less good for the summer).

When the model response (Fig. 17) is compared with the 500 mbar climatology (Fig. 18), we note that:

a) The closed cyclonic cell in the trough over North America lies at the south of the Hudson Bay instead of at its north-northeast as observed.

b) It is slightly off-centered from the North Pole that the computed free surface height field has its deepest depression although no depression is observed in this region.

c) The observed trough over the east of the asiatic continent is badly represented. Instead of a single trough over the Kamchatka and the Western Pacific, the computed solution shows a trough which, at the latitude of the Sakhalin Island, divides into two branches: one over China, the other over the Pacific.

d) On the 500 mb climatological chart, the Hudson Bay trough is more pronounced than the trough off the east coast of Asia while the model produces equally marked troughs.

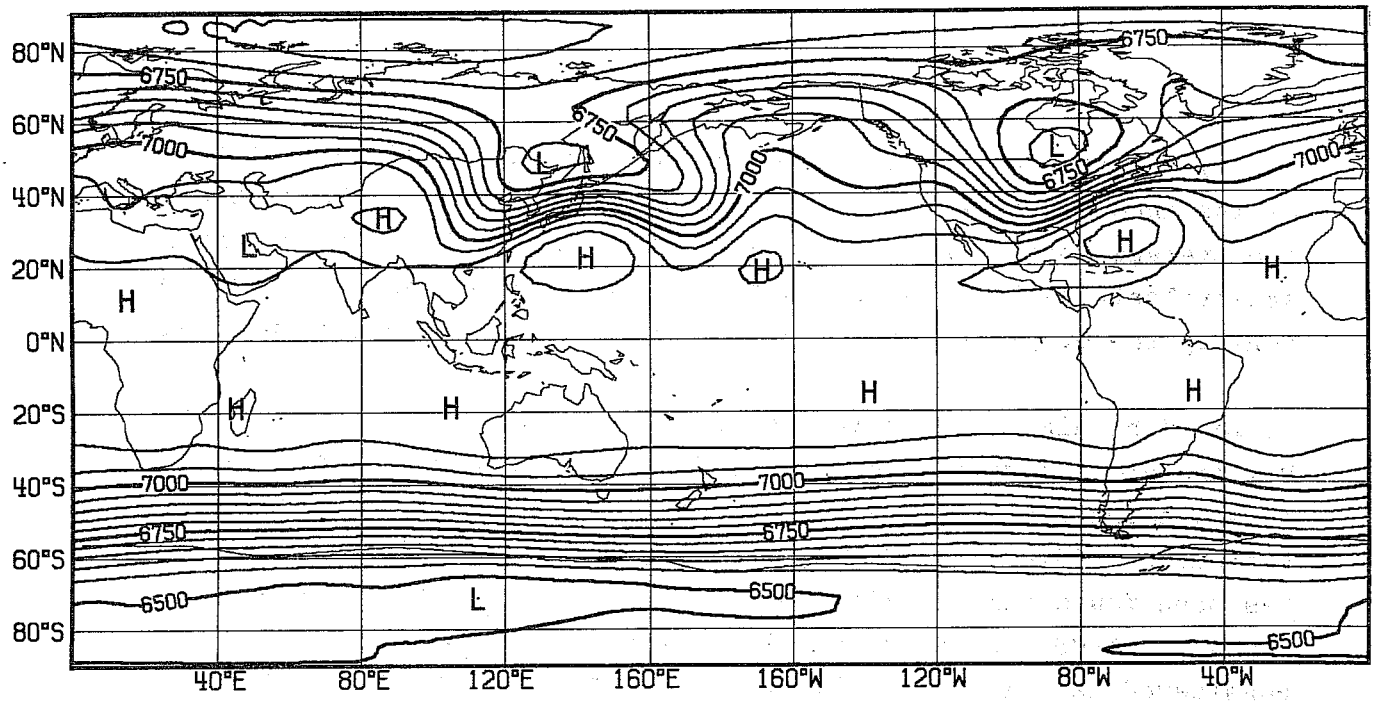

Fig. 15 Response of the free surface to the planetary orographical forcing after 10 days. Heights in m.

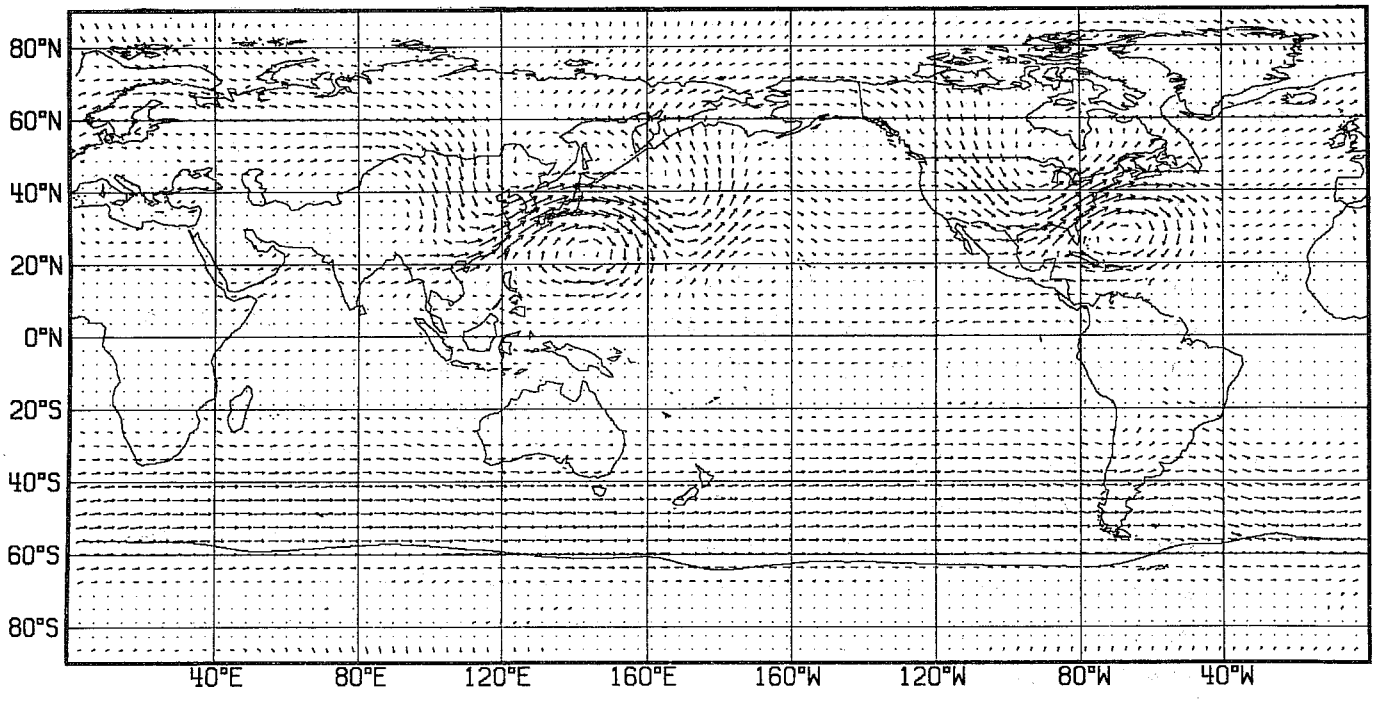

Fig. 16 Response of the wind field to the planetary orographical forcing after 10 days.

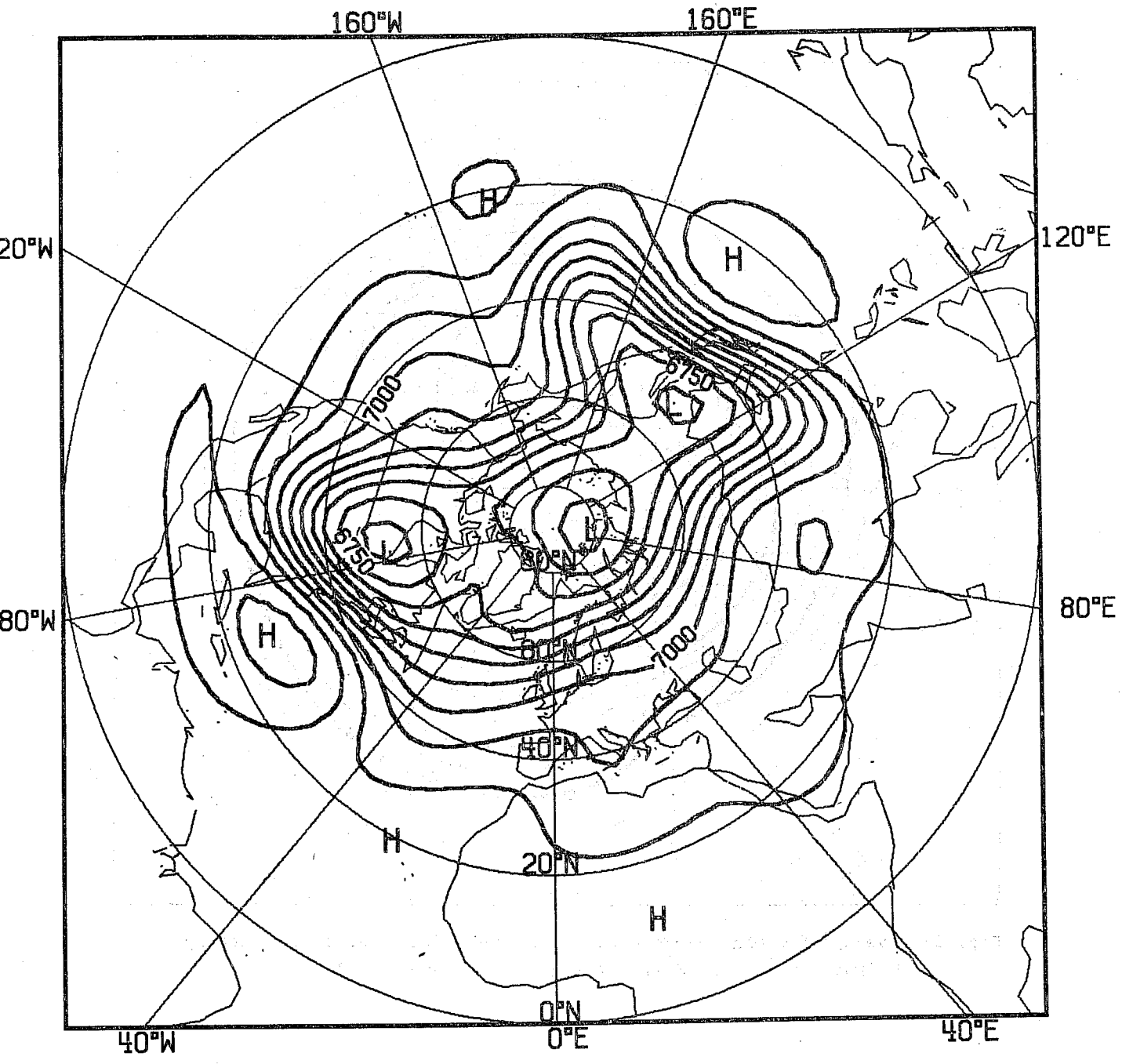

Fig. 17 Same as Fig. 15 but on a stereographic projection of the North Hemisphere.

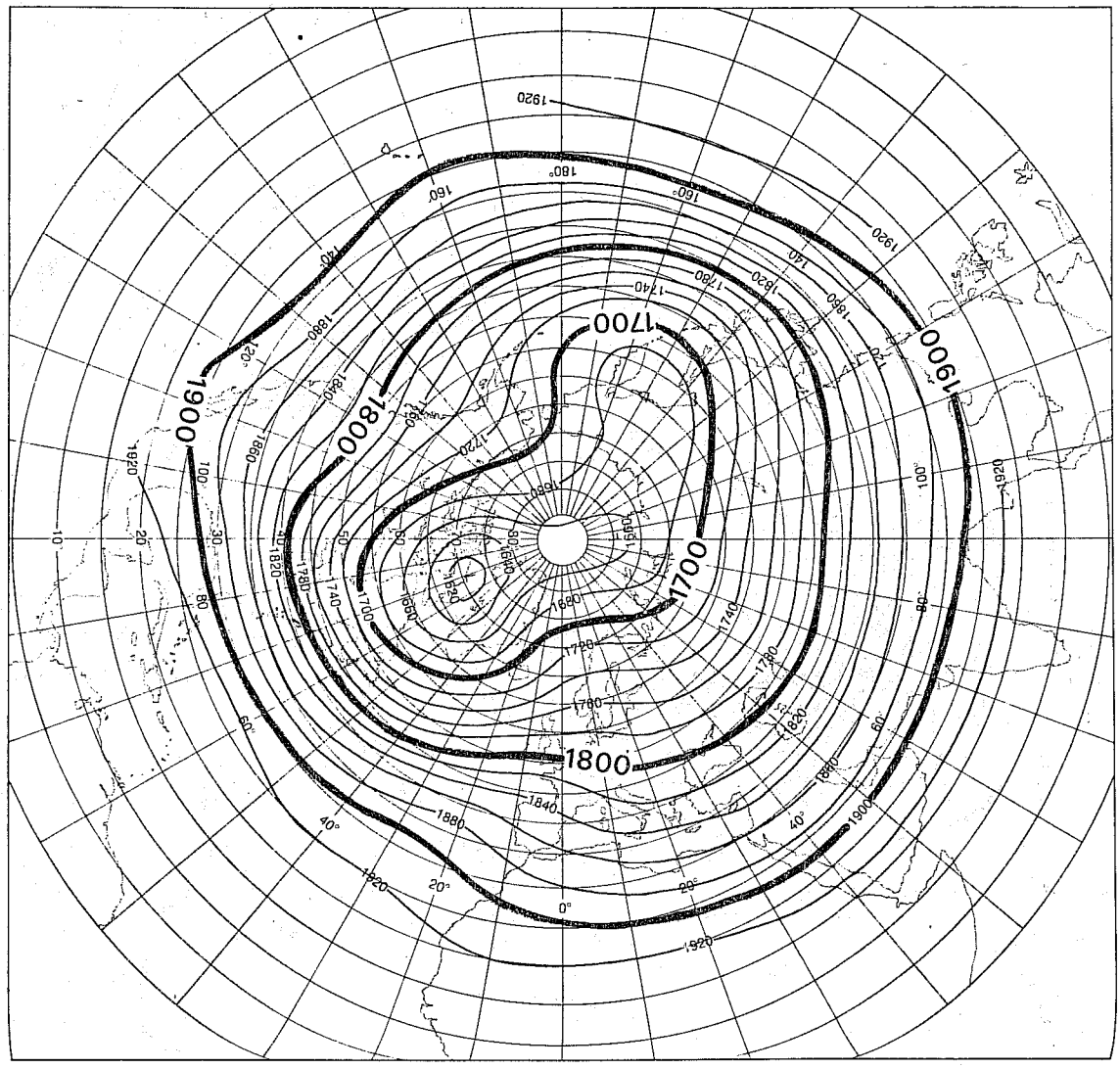

Fig. 18 Average 500-mbar surface of the Northern Hemisphere for January. Heights in tens of feet. (From the U.S. Weather Bureau).

More generally, it can be said that the observed January 500 mb pattern is much smoother and more zonal than the result of the model. If integration is pursued beyond 10 - 12 days, the zonal flow in the Northern Hemisphere breaks in several cells and loses more and more resemblance with climatology.

The response to the global orography forcing obtained by Grose and Hoskins (see Fig. 6a in Grose and Hoskins, 1979) approaches the climatology better than the response presented here (Fig. 18). But their model also produces an unexisting depression slightly off-centered from the North Pole. But the two main troughs (the Hudson Bay one and the one off the east coast of Asia) are represented with great conformity.

2.5 Concluding remarks

Although Grose and Hoskins have used the 300 mbar zonally averaged wind together with a mean free surface height of 10 km while here the 500 mbar wind has been used for a 7 km deep atmosphere, it is interesting to see that both works show similar results. But when these two authors use the climatological 500 mbar flow, but retaining a depth of 10 km, the response they obtain deviates strongly from the climatology. (Four large troughs are produced in this case as Fig. 7a in Grose and Hoskins (1979) shows). This is a consequence of the basic shortcoming of the shallow water equations when applied to the atmosphere, a shortcoming already implied by their name: their "hydraulic" character which makes their solution very dependent on the depth of the fluid.

Acknowledgements

The author gratefully acknowledges the suggestion of L. Bengtsson to undertake this investigation and thanks him for his stimulating guidance throughout. My thanks are also due to B. Hoskins who also encouraged me to start this work and to A. Simmons and S. Tibaldi for the interest they have shown.

References

Asselin, R., 1972: Frequency Filter for Time Integrations. Mon. Wea. Rev., 100, 487-490.

Barry, R. and Perry, A., 1973: Synoptic Climatology. Methuen & Co. Ltd., London, p. 77.

Burridge, D.M. and Haseler, J., 1977: A Model for Medium Range Weather Forecasts - Adiabatic Formulation. ECMWF, Technical Report No. 4.

Dzerdzeevskii, B. and Pogosyan, P., 1968: General Circulation of the Atmosphere. Izdatel'stvo "Nauka", Moskva, p. 241

Grose, W. and Hoskins, B., 1979: On the Influence of Orography on Large-Scale Atmospheric Flow. J. Atmos. Sci., 36, 223-234.

Haltiner, G.J. and Martin, F.L., 1957: Dynamical and Physical Meteorology. McGraw-Hill Book Co., pp. 375-376.

Haseler, J. and Burridge, D., 1977: Documentation for the ECMWF Grid Point Model. ECMWF, Internal Report No. 9.

Haurwitz, B., 1940: The Motion of Atmospheric Disturbances. J. Marine Res., 3, 35-50.

Holloway, J. and Manabe, S., 1971: Simulation of Climate by a Global General Circulation Model. Mon. Wea. Rev., 99, 335-370.

Kasahara, A., 1966: The Dynamical Influence of Orography on the Large-Scale Motion of the Atmosphere. J. Atmos. Sci., 23, 259-271.

Neiburger, M., Edinger, J. and Bonner, W., 1971: Understanding Our Atmospheric Environment. W.H. Freeman & Co., p. 128.

Newell, R. and al., 1969: The Energy Balance of the Global Atmosphere. Joint Conference on the Global Circulation of the Atmosphere held in London, 25-29 August 1969. Edited by G. Corby, Royal Meteorological Society.

Oort, A.H. and Rasmusson, E.M., 1971: Atmospheric Circulation Statistics. NOAA, Professional Paper 5.

Sadourny, R., 1975a: The Dynamics of Finite-Difference Models of the Shallow-Water Equations. J. Atmos. Sci., 32, 680-689.

Sadourny, R., 1975b: Compressible Model Flows on the Sphere. J. Atmos. Sci., 32, 2103-2110.